A Regional Model Simulation of the 1991 Severe Precipitation Event over the Yangtze–Huai River Valley. Part II: Model Bias

WEI GONG AND WEI-CHYUNG WANG

Atmospheric Sciences Research Center, University of Albany, State University of New York, Albany, New York

(Manuscript received 6 July 1998, in final form 12 February 1999)

ABSTRACT

This is the second part of a study investigating the 1991 severe precipitation event over the Yangtze–Huai River valley (YHRV) in China using both observations and regional model simulations. While Part I reported on the Mei-yu front and its association with large-scale circulation, this study documents the biases associated with the treatment of the lateral boundary in the regional model. Two aspects of the biases were studied: the *driving field*, which provides large-scale boundary forcing, and the *coupling scheme*, which specifies how the forcing is adopted by the model. The former bias is defined as *model uncertainty* because it is not related to the model itself, while the latter bias (as well as those biases attributed to other sources) is referred to as *model error*. These two aspects were examined by analyzing the regional model simulations of the 1991 summer severe precipitation event over YHRV using different driving fields (ECMWF–TOGA objective analysis, ECMWF reanalysis, and NCEP–NCAR reanalysis) and coupling scheme (distribution function of the nudging coefficient and width of the buffer zone). Spectral analysis was also used to study the frequency distribution of the bias.

The analyses suggest that the 200-hPa winds, 500-hPa geopotential height, and 850-hPa winds and water vapor mixing ratio, which have dominant influences on Mei-yu evolution, are sensitive to large-scale boundary forcing. In particular the 500-hPa geopotential height, and 850-hPa water vapor mixing ratio near the Tibetan Plateau and over the western Pacific Oceans are highly dependent on the driving field. On the other hand, the water vapor in the lower troposphere, wind at all levels, and precipitation pattern are much more affected by the treatment of nudging in the coupling scheme. It is interesting to find that the two commonly used coupling schemes, the lateral boundary coupling and the spectral coupling, provide similar large-scale information to the simulation domain when the former scheme used a wider buffer zone and stronger nudging coefficient. Systematical model errors, existing in the north of the simulation domain, are caused by the overprediction of low-level inversion stratiform clouds.

The analyses further indicate that the model mesoscale signal is not significantly influenced by the different treatments of the nudging procedure. However, it is also shown that the model performance, especially the monthly mean precipitation and its spatial pattern, is substantially improved with the increase of buffer zone width and nudging coefficient.

1. Introduction

In Wang et al. (2000), the State University of New York at Albany (SUNYA) Regional Climate Model (RCM) was used to simulate the precipitation evolution and the associated large-scale circulation of the 1991 summer monsoon over East Asia. This study examines the biases related to the RECM simulations. There are many causes for the model biases, including the model numerics, physical parameterization, and continued update of the lateral boundary condition. As pointed out by Anthes et al. (1989), the latter can introduce large bias, which is perhaps even more serious than the initialization or spinup during long integration. Here, we examine the causes for the SUNYA-RCM bias, with focus on those associated with the use of lateral boundary to drive the regional model. In general, the model biases associated with the lateral boundary can be attributed to two sources: the *driving field*, which describes the large-scale lateral boundary forcing, and the *coupling scheme*, which specifies how the forcing is used as input to the regional model.

The driving field is usually derived from two types of data, either the objective analysis (Giorgi et al. 1993a) or output from the general circulation model (GCM) simulations (Walsh and Watterson 1997). Since the driving field is externally specified, we define the model biases associated with the driving field as model *uncertainties*. There were several studies that examined these model uncertainties. For example, in a predictability study, Vukicevic and Errico (1990) used a mesoscale model to show that perturbations in the driving

Corresponding author address: Dr. Wei-Chyung Wang, Atmospheric Sciences Research Center, SUNY at Albany, 251 Fuller Rd., Albany, NY 12203.
E-mail: wang@climate.cestm.albany.edu

field would contaminate the regional model internal solution rather quickly, within 3–6 h. More recently, Waldron et al. (1996) found that 12-h simulations in a limited-area model are sensitive to the driving field. For a longer period, Giorgi (1990) showed that after 1-month integration, the National Center for Atmospheric Research (NCAR) Regional Climate Model version 1 simulated large-scale fields were not substantially different from those of the GCM.

There are several objective analyses that can be used as driving fields, including the European Centre for Medium-Range Weather Forecasts–Tropical Ocean Global Atmosphere (ECMWF–TOGA) analysis and reanalysis, the National Centers for Environmental Prediction (NCEP)–NCAR analysis and reanalysis, and National Aeronautics and Space Administration/Data Acquisition Office (NASA/DAO) reanalysis. However, as shown in Trenberth and Guillemot (1995), Min and Schubert (1997), and Bony et al. (1997), substantial differences exist among these objective analyses, in particular in low-level jet and water vapor flux, which play important roles in heavy precipitation events over East Asia (Tao and Chen 1987) and in North America (Mo et al. 1995). It is therefore necessary to quantify the model uncertainties associated with the different driving fields.

On the other hand, the coupling scheme, which specifies how the large-scale forcing described by the driving fields is being used in the model simulations of prognostic variables, also plays an important role. One commonly used and easily implemented coupling scheme is the lateral boundary coupling (LBC; see Davies 1976), which was recently reviewed by Warner et al. (1997). The most notable deficiency of this scheme is that the large-scale forcing is present only at the lateral boundaries, and therefore the regional climate model atmospheres may drift during integration, especially for large simulation domain (Sasaki et al. 1995; Pan et al. 1999). To eliminate the problem, the spectral boundary coupling (SBC) scheme was developed by Kida et al. (1991), Sasaki et al. (1995), and Waldron et al. (1996). In this scheme, the large-scale information from the driving field and small-scale information from the regional model simulations are combined over the entire domain (see Fig. 3 of Kida et al. 1991). This treatment, if used frequently (e.g., for half a day or even at each integration time step), can eliminate the model drifting (Sasaki et al. 1995). However, the SBC scheme has its implicit problems, such as the demand for more computational effort, and the discontinuity in prognostic variables before and after the SBC is applied due to the difference in large-scale information between the driving field and model. Perhaps, the most serious one is that the errors inherently existing in the driving fields may be carried into the simulation domain and thus lead to worse results than those using the LBC scheme.

The present paper is the second part of the study evaluating the performance of the RCM in simulating the 1991 summer monsoon over East Asia. While Part I (Wang et al. 2000) documents the capability of the RECM in simulating the precipitation evolution and its associated circulation components, this study focuses on the causes for the model biases with focus on the lateral boundary conditions. Note that the RCM simulation results in Part I are based on the best model configurations concluded here. Section 2 describes the experiment and diagnostic method. Because the objective analyses provide the large-scale information, we also compare them with the model simulated large-scale fields. In section 3, we analyze the model uncertainty associated with the different driving fields. The results of model sensitivity to the coupling scheme are summarized in section 4, and conclusions and discussion are given in section 5.

2. Model simulations

a. Regional model

As summarized in Wang et al. (2000), the SUNYA–RCM was used to simulate the 1991 summer severe precipitation event over Yangtze–Huai River valley (YHRV) using the ECMWF–TOGA objective analysis as the driving field. It is shown that the simulated precipitation and surface air temperature are in reasonably good agreement with available observations. In this study, the basic model characteristics, including the integration domain, horizontal grids and vertical levels, and model numerical schemes and physical parameterization, are the same as in Wang et al. (2000), except for those explicitly indicated below.

The diagnostic cloud–radiation parameterization, documented in Liang and Wang (1995), is based on Slingo and Slingo (1991) with some refinements. As in the original parameterization, the amounts of four types of clouds—convective cloud, anvil cirrus, stratiform cloud, and inversion stratus—were diagnosed following the original scheme. For the radiation calculation, stratiform cloud and inversion stratus are combined into a single genus. Convective cloud forms as a vertical tower of all continuous convective layers, while anvil cirrus occupies the top layer of deep convection and inversion stratus occurs in one near-surface layer. There are several refinements including: the convective cloud's dependence on convective precipitation, the formation of anvil cirrus when convective cloud cover is greater than 0.1 for altitudes above 650 hPa, the inversion stratus dependence on layer stability given by Kiehl (1994) without the pressure factor that accounts for the transition between marine stratus and trade cumulus, and stratiform cloud formation in any model layer when relative humidity exceeds a threshold value from 0.9 at the surface to 0.7 above 800 hPa. The simulated stratiform clouds were found to be in good agreement with the data from the southern Great Plains of the atmosphere radiation measurement (Dudek et al. 1996). However, the parameterization is found to be sensitive

TABLE 1. Designation of sensitivity experiments for different driving fields derived from objective analyses. In these experiments, an 18-gridpoint buffer zone and exponential distribution function for nudging coefficient are applied, and inversion stratus is included in the diagnosic cloud–radiation parameterization.

Designation	Driving field
A	ECMWF–TOGA analysis
B	ECMWF reanalysis
C	NCEP–NCAR reanalysis

to both the geographical regions and the model horizontal resolution.

To study the model uncertainty, we conduct simulations using three sets of driving fields: the ECMWF–TOGA analysis, which was used in Wang et al. (2000), the ECMWF reanalysis, and the NCEP–NCAR reanalysis. These driving fields and the corresponding model simulations are designated as A, B, and C, respectively (see Table 1). All three objective analyses used in this paper have horizontal resolution of $2.5^\circ \times 2.5^\circ$ (about 280 km in north–south direction), while in the vertical, the ECMWF–TOGA analysis has 15 pressure levels, and both ECMWF reanalysis and NCEP–NCAR reanalysis have 17 pressure levels. The above data are linearly interpolated onto the RCM grid points and integration time steps. A detailed description of the above interpolation scheme and its influence on the model simulation can be found in Leung et al. (1999). Because of a lack of observations, the objective analyses are also used as references for comparing the model errors or uncertainties described in sections 3 and 4.

We use the *relaxation scheme* of LBC to conduct simulations for the cases A, B, and C. In this scheme, the model's prognostic variables were nudged toward the driving fields in the lateral buffer zone with a specified distribution function for the nudging coefficient [weighting factor; see (11) of Giorgi et al. (1993b)]. In general, the buffer zone width is defined as the number of grid points from the lateral boundaries, while the nudging coefficient provides the amount of information conveyed to the grid points within the buffer zone. There are several choices for the nudging coefficient of the relaxation scheme. For example, Anthes et al. (1987) adopted a linear distribution function for nudging coefficient in a 5-gridpoint buffer zone (but actually only the coefficients for the middle three gridpoints are effective in nudging). This choice of nudging coefficients may cause a drift of the simulations for long time integration (Kida et al. 1991), and thus induce spurious precipitation near the lateral boundary as the result of a large difference between the model variable and driving field (Giorgi et al. 1993a). To overcome this deficiency, an exponential decay function (horizontally) and the nudging increases with altitude was proposed by Giorgi et al. (1993b). In so doing, the large difference between the model and the driving field within the buffer zone, especially at upper model layers, can be eliminated because of the much smoother transition. The exponential function, however, requires a much wider buffer zone to make the coefficient at the innermost grid point in the buffer zone small enough to avoid discontinuity.

For the simulations with the three driving fields, we adopted the exponential distribution function described in Giorgi et al. (1993b). An 18-gridpoint buffer zone was used so that it is wide enough to provide a smooth transition, but still gives a fairly large simulation domain to cover the Mei-yu evolution (see Fig. 4 of Wang et al. 2000). In addition, the focused area YHRV located in the center of the domain will have the least effect from the driving fields. Note that for all three cases, we used the same diagnostic cloud–radiation parameterization as in Dudek et al. (1996) while model sensitivity experiments discussed in section 4 were conducted by excluding the inversion stratus.

b. Analysis of model biases

Ideally, the model biases can be identified by directly comparing simulation and observation. However, a lack of high (both temporal and spatial) resolution observations make it difficult to accomplish. This is especially true over oceans and mountains (e.g., Tibetan Plateau) where observations are sparse and sometimes nonexistent. The global objective analysis, although based on model, perhaps becomes the only available complete dataset for comparison purposes. However, note that the objective analysis is adequate for large-scale circulation information but not for the small-scale climate characteristics because of its coarse resolution. Therefore, the method used to derive model bias presented below is aimed at the large-scale information of both model variable and objective analysis.

For a given atmospheric field, it is typical to use the first few components of the Fourier series to represent the large-scale information. However, given the small domain size of the regional model, Errico (1985) and Tatsumi (1986) suggested that those components with wavelengths longer than the domain size, refereed as the ''additional bases,'' need to be removed before the spectral transform is applied. The elimination of these bases also allows the remaining field to satisfy the periodical condition. The procedure was used by Kida et al. (1991) and Sasaki et al. (1995). We follow this idea, taking the bases as the linear trend calculated using the boundary values of the individual fields (Errico 1985).

As an example, a field $F_{i,j}$ can be expanded into double Fourier series after subtracting the linear slope $Fb_{i,j}$ (see Errico 1985 for details). Here, subscripts i and j denote the indices of the grid point starting from southern and western boundaries of the simulation domain, and N_I and N_J are the total number of grid points in zonal and meridional directions. The large-scale part of the field $Fl_{i,j}$ is then the sum of the first few components (lower wavenumbers) and the linear slope, $Fb_{i,j}$, as

$$Fl_{i,j} = Fb_{i,j} + \sum_k \sum_l C_{k,l} \times \exp\left\{-2\pi\sqrt{-1} \times \left[\frac{k(i-1)}{N_I - 1} + \frac{l(j-1)}{N_J - 1}\right]\right\}, \quad (1)$$

where k and l are wavenumbers ($-N_I/2 \le k \le +N_I/2$; $-N_J/2 \le l \le +N_J/2$), respectively, and k and l satisfy a relation that is used to determine the summation limit of (1) and will be given below. Here $C_{k,l}$ is the two-dimensional Fourier spectral coefficient and describes the amplitude of the wave, and given as

$$C_{k,l} = \frac{1}{(N_I - 1)(N_J - 1)} \sum_{j=1}^{N_J-1} \sum_{i=1}^{N_I-1} (F_{i,j} - Fb_{i,j}) \times \exp\left\{2\pi\sqrt{-1} \times \left[\frac{k(i-1)}{N_I - 1} + \frac{l(j-1)}{N_J - 1}\right]\right\}. \quad (2)$$

Expression (1) describes that the large-scale part $Fl_{i,j}$ is composed of the component $Fb_{i,j}$ with wavelength beyond the domain size, and the other components with wavelength below the domain size. As in Eq. (6) of Errico (1985), the minimum wavenumber Δk that can be resolved by the model grids is given by

$$\Delta k = \frac{2\pi}{[\text{Max}(N_I, N_J) - 1]\Delta x}, \quad (3)$$

where Δx is model grid spacing.

Thus, the corresponding wavelength l_c for directionally independent scalar wavenumber $k_c\Delta k$ [$k_c = 1, \ldots, \frac{1}{2}\,\text{Max}(N_I, N_J)$] is given by

$$l_c = \frac{2\pi}{k_c\Delta k}. \quad (4)$$

The upper limit of k_c could be determined by the horizontal resolution of the objective analysis. For example, ECMWF–TOGA analysis used here is at 2.5° × 2.5° (approximately 280 km in south–north direction), then we have $k_c = 18$ according to (3) and (4). In this study, we are concerned more about the several longest wavelengths, at which most of the large-scale information is stored. Components at these wavelengths are crucial in describing the difference of model-simulated variable from the objective analysis. Therefore, we select $k_c = 5$ (approximately corresponding to wavelength 996 km for the domain size and horizontal resolution) as the upper limit, which is the typical cyclone scale at midlatitudes and can be well resolved by GCMs. Thus, the summation limits, for k and l in (1), satisfy [according to Eq. (5) of Errico 1985]:

$$\left(\frac{k}{N_I - 1}\right)^2 + \left(\frac{l}{N_J - 1}\right)^2 \le \left[\frac{5 + \frac{1}{2}}{\text{Max}(N_I, N_J) - 1}\right]^2. \quad (5)$$

After the large-scale parts of both objective analysis and model-simulated fields are obtained, three types of quantities are used to describe the model bias. The first quantity is the monthly mean of absolute value of daily difference, defined as *monthly mean absolute difference*, which reflects the daily variability of model bias. The second quantity is the monthly mean of daily bias, defined as *monthly mean difference*. If the monthly mean absolute bias matches the magnitude of the monthly mean bias, the model has systematic bias in its climate state. The third quantity is the time variation of model bias, defined as the root-mean-square (rms) bias:

$$\text{rms} = \sqrt{\overline{(Fl_m - Fl_o)^2}}, \quad (6)$$

where subscripts *m* and *o* represent the model-produced field and objective analysis, respectively, and the overbar denotes spatial average over the *inner domain*, defined to be the total number of grid points excluding the 18 grid points near the lateral boundaries. Expression (6) is also used to calculate the rms error in simulated precipitation surface air temperature against the observations. In this case, the overbar denotes the average over the stations in a given region.

3. Model uncertainties associated with the driving field

As discussed in Wang et al. (2000), our analyses focus on 200-hPa winds, 500-hPa geopotential height, and 850-hPa water vapor mixing ratio and winds, because of their important roles in influencing the evolution of the Mei-yu system and precipitation over YHRV. We show only the May simulation since similar results are found for other summer months. Note again that the fields presented here are the large-scale information through retaining the several longest spectral components together with the field of linear slope.

Figure 1 shows the monthly mean absolute differences in the 500-hPa geopotential height between the model simulation and the corresponding objective analysis for the three cases, A, B, and C, respectively. One notable feature is that similar differences exist in both the magnitude and pattern in the northern part of the domain for all three cases. Therefore, these systematic differences, attributed to the model dynamics and/or physical parameterizations, and/or by the coupling scheme, can be categorized as ''model error.'' An examination of the monthly mean difference in this field (not shown) indicates that this model error leads to a decrease in geopotential gradient which, in turn, affects the mid- and lower-tropospheric circulation as well as the region where heavy precipitation occurred. On the other hand, the large difference found near the Tibetan Plateau in case A (to a lesser extent in case B but not in case C) is related to the differences in the driving fields, and thus can be categorized as ''model uncertainty.''

Note that the magnitude of the model uncertainty, although only for a small area, is similar to those of model error. A close examination of the three objective

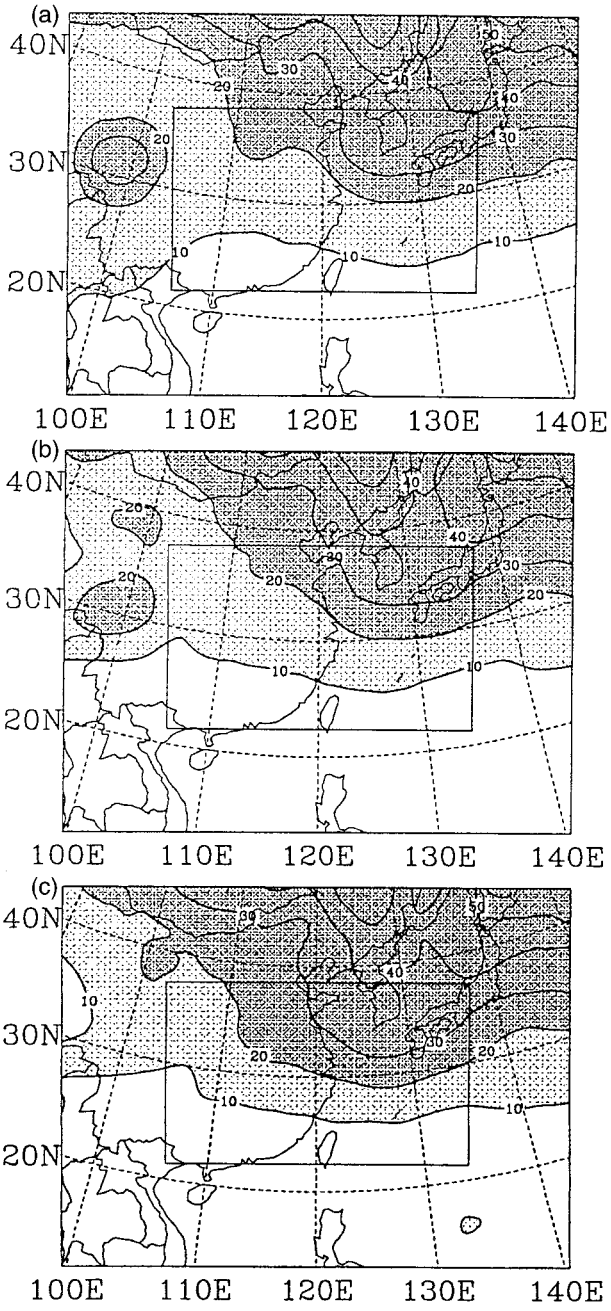

FIG. 1. The May monthly mean absolute value of daily differences in the large-scale component of the 500-hPa geopotential height (gpm) between the model simulation and the corresponding objective analysis. The three cases, (a) case A, (b) case B, and (c) case C, are listed in Table 1. Contours greater than 10 (20) gpm are lightly (densely) shaded. The area between the inner and outer frames denotes the 18-gridpoint buffer zone.

analyses indicates that substantial differences exist over the western part of the simulation domain, especially near the Tibetan Plateau. The difference between ECMWF–TOGA analysis and NCEP–NCAR reanalysis (shown in Fig. 2) is particularly large. This difference may reflect the different treatment of the Tibetan Plateau

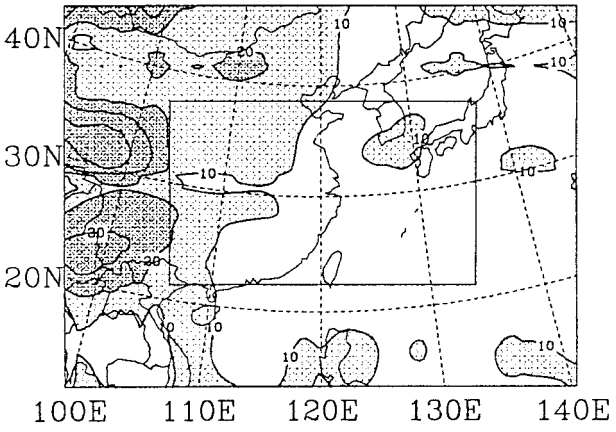

FIG. 2. The May monthly mean absolute value of daily differences in the large-scale component of the 500-hPa geopotential height (gpm) between ECMWF–TOGA analysis and NCEP–NCAR reanalysis. Contours greater than 10 (20) gpm are lightly (densely) shaded.

in the models by which the objective analyses were generated. Other possible sources include the different spatial and temporal interpolation schemes during the preprocessing of lateral boundary conditions and post-processing of regional model outputs. Note that these model uncertainties in the lateral buffer zone, for each case, are less than the corresponding differences between the objective analyses themselves, thus suggesting that differences in the driving fields indeed pass onto the simulation domain.

Figure 3 shows the monthly mean absolute difference in 850-hPa zonal wind between simulation and objective analysis for case A. The similar model error as that found in the 500-hPa geopotential field is not surprising because of the close relationship between the two fields. Over a relatively small area near the Tibetan Plateau, a large difference is found for this case, but not for cases

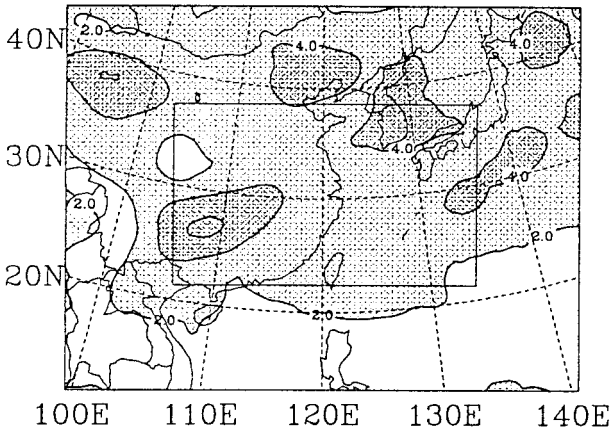

FIG. 3. The May monthly mean absolute value of daily differences in the large-scale component of 850-hPa zonal wind (m s^{-1}) between the model simulation and the corresponding objective analysis for case A. Contours greater than 1.0 (2.0) m s^{-1} are lightly (densely) shaded.

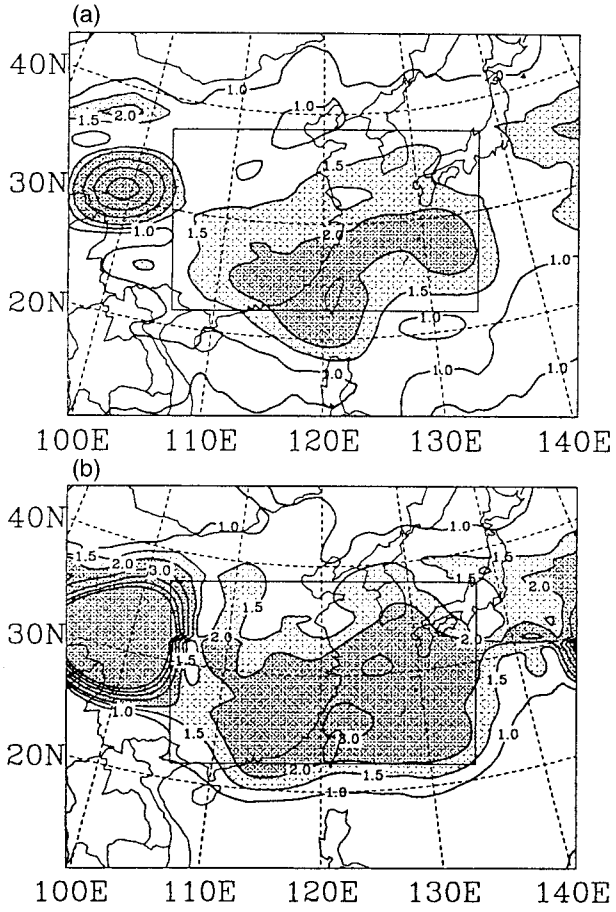

FIG. 4. The May monthly mean absolute value of daily differences in large-scale component of 850-hPa water vapor mixing ratio (g kg^{-1}) between the model simulation and the corresponding objective analysis. The two cases, (a) case A, and (b) case C, are listed in Table 1. Contours greater than 1.5 (2.0) g kg^{-1} are lightly (densely) shaded.

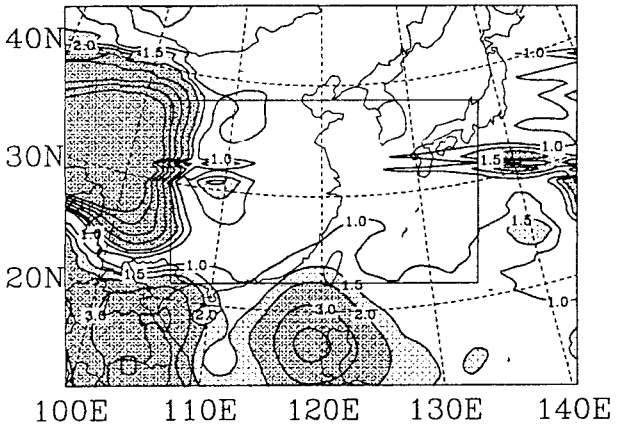

FIG. 5. Same as in Fig. 2 except for 850-hPa water vapor mixing ratio (g kg^{-1}). Contours greater than 1.5 (2.0) g kg^{-1} are lightly (densely) shaded.

B and C (not shown), and it again reflects the uncertainties of the driving fields. The monthly mean absolute differences in 850-hPa water vapor mixing ratio between model simulation and objective analysis for cases A and C are shown in Fig. 4. A persistent difference over southeast China and the nearby oceanic area is found; a similar result exists for case B (not shown). The results of monthly mean difference (not shown) indicate a negative error (underestimate) of the water vapor. This feature is also consistent with the smaller mean precipitation over YHRV (Wang et al. 2000). Another significant difference in water vapor mixing ratio between simulated and analyzed data is found near the Tibetan Plateau, but the magnitude of difference is substantially different among the three cases, thus again indicating the model uncertainty. Indeed, the difference in the driving fields between ECMWF–TOGA analysis and NCEP–NCAR reanalysis, shown in Fig. 5, reflects these characteristics. In addition, there are also two areas in the south where large differences exist. However, these differences are not reflected in the simulations shown in Fig. 4, thus implying the damping effect of the coupling scheme in the buffer zone.

We have also examined in detail other large-scale fields that affect the Mei-yu system. In summary, in the northern part of the domain, we found substantial differences in the 850-hPa meridional wind, and 200-hPa zonal and meridional winds between the simulation and the corresponding analysis for all the three cases. These differences are basically model errors because they do not vary greatly among these cases while the differences among the objective analyses are also small.

Having examined the model bias, we can evaluate the model uncertainties due to the driving fields in contrast to the model error. For the three simulation cases, the largest differences are found between case A/or B and case C. This is undoubtedly due to the relatively smaller difference between ECMWF–TOGA analysis and ECMWF reanalysis. Therefore, our analyses focus on cases A and C. The difference is still calculated based upon the large-scale part of the field although the total difference (i.e., when all the spectral components are included) is generally larger, by up to 20%–30%. Figure 6 shows the monthly mean absolute difference in 500-hPa geopotential height between cases A and C. Maximum differences larger than 10 gpm are found along the western and southern boundaries as well as south of the Korean Peninsula; these also occur in the monthly mean difference with the same magnitude but opposite sign (not shown). As a result, the gradient of subtropical high in case A is different from that in case C, resulting in two different circulation patterns associated with geostrophic balance. Note also in Fig. 6 that maximum difference in the southern Korean Peninsula and south of it coincides with the location where the model error peaks. As will be discussed in section 4, this maximum is related to the uncertainty of the driving field.

The simulated monthly precipitation pattern for case A is different from case C in that the latter rain belt is located farther north (not shown). Such a difference is

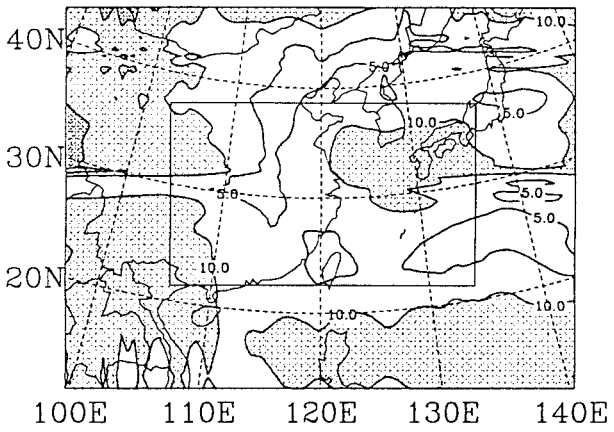

FIG. 6. The May monthly mean absolute value of daily differences in the large-scale component of 500-hPa geopotential height (gpm) between the model simulations of cases A and C. Contours greater than 10 (20) gpm are lightly (densely) shaded.

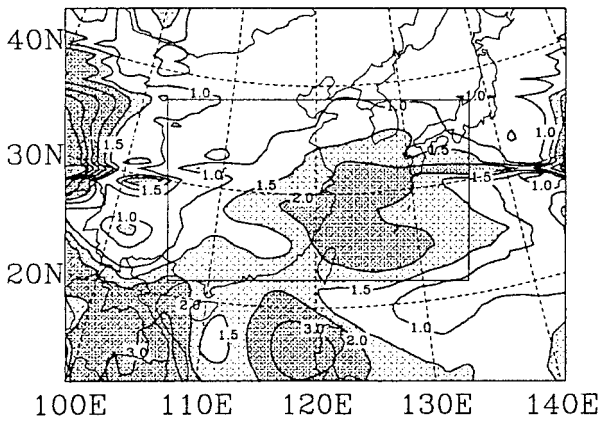

FIG. 7. Same as in Fig. 6 except for 850-hPa water vapor mixing ratio (g kg^{-1}). Contours greater than 1.5 (2.0) g kg^{-1} are lightly (densely) shaded.

partially caused by the difference in water vapor, as shown in Fig. 7 of the 850-hPa water vapor mixing ratio. A large difference is located over the oceanic area east of YHRV where model error is also large. This point can be further illustrated by comparing (shown in Fig. 8) the time variation of daily rms difference of water vapor mixing ratio at each model level over the inner domain between the model simulation and ECMWF–TOGA analysis for case A, and between cases A and C. Comparable differences are found for the two comparisons and the maximum differences are near the top of the boundary layer. The latter feature is related to different boundary layer parameterization used in the RCM and in the models used to generate the analysis/reanalysis. Therefore, the different precipitation pattern may be illustrated partly by the fact that the largest differences in water vapor are located at levels where both convective and large-scale condensation are most active.

4. Effects of coupling schemes

The influence of the coupling scheme was illustrated by two sets of sensitivity experiments using ECMWF–TOGA analysis as the driving field. In the first set, case A was rerun with a 5-gridpoint buffer zone width and a linear distribution of nudging coefficients (case L5I in Table 2). As shown in Fig. 9, the nudging coefficients for this case decrease rapidly from 1.0 at the outermost grid point of the buffer zone to 0 at the innermost grid point. Note that, as discussed in section 3, case A is based on an 18-gridpoint buffer zone and exponentially distributed nudging coefficients. It is obvious that exponentially distributed nudging coefficients decrease much more slowly than the linear distribution function. Moreover, as suggested by Giorgi et al. (1993b), the nudging coefficients increase with height so that the driving field has more influence on the model prognostic variables in the free troposphere.

In the second set, we repeated cases A and L5I by removing the inversion stratus, denoted, respectively, by E18 and L5 (see Table 2), because it produces excessive low-level clouds in case A. In the diagnostic cloud–radiation parameterization, this inversion stratus forms over the area with greater atmospheric stability, especially under the western Pacific subtropical high and in the northern part of the simulation domain. The atmosphere in the latter area was generally stable because the unstable monsoon flow did not reach this region for most of the time from May to July. Comparison among the four cases from the two sets of experiments can identify the effects of the coupling schemes as well as on how the low-level stratus affect the model errors.

a. Large-scale circulation

Figure 10a shows the monthly mean absolute difference in 500-hPa geopotential height between the simulation and ECMWF–TOGA analysis for case L5I. The results indicate that the model error in case A is not sensitive to the coupling scheme especially over the northern part of the domain. However, when the inversion stratus was removed (cases E18 and L5; Fig. 10b and 10c), the model error was significantly reduced for both coupling schemes. These suggest that the model error in case A is mainly due to the excessive low cloud amounts, which decrease the downward solar radiation reaching the surface and thus induce a cooling effect. In addition, they also change the radiative heating profile and radiative fluxes in the atmosphere, through cloud–radiation interaction.

Although the largest inversion cloud amount is simulated over the region of the western Pacific subtropical high where atmospheric relative humidity is large, the largest effect is found in the northern part of the simulation domain. This phenomenon is related to the dif-

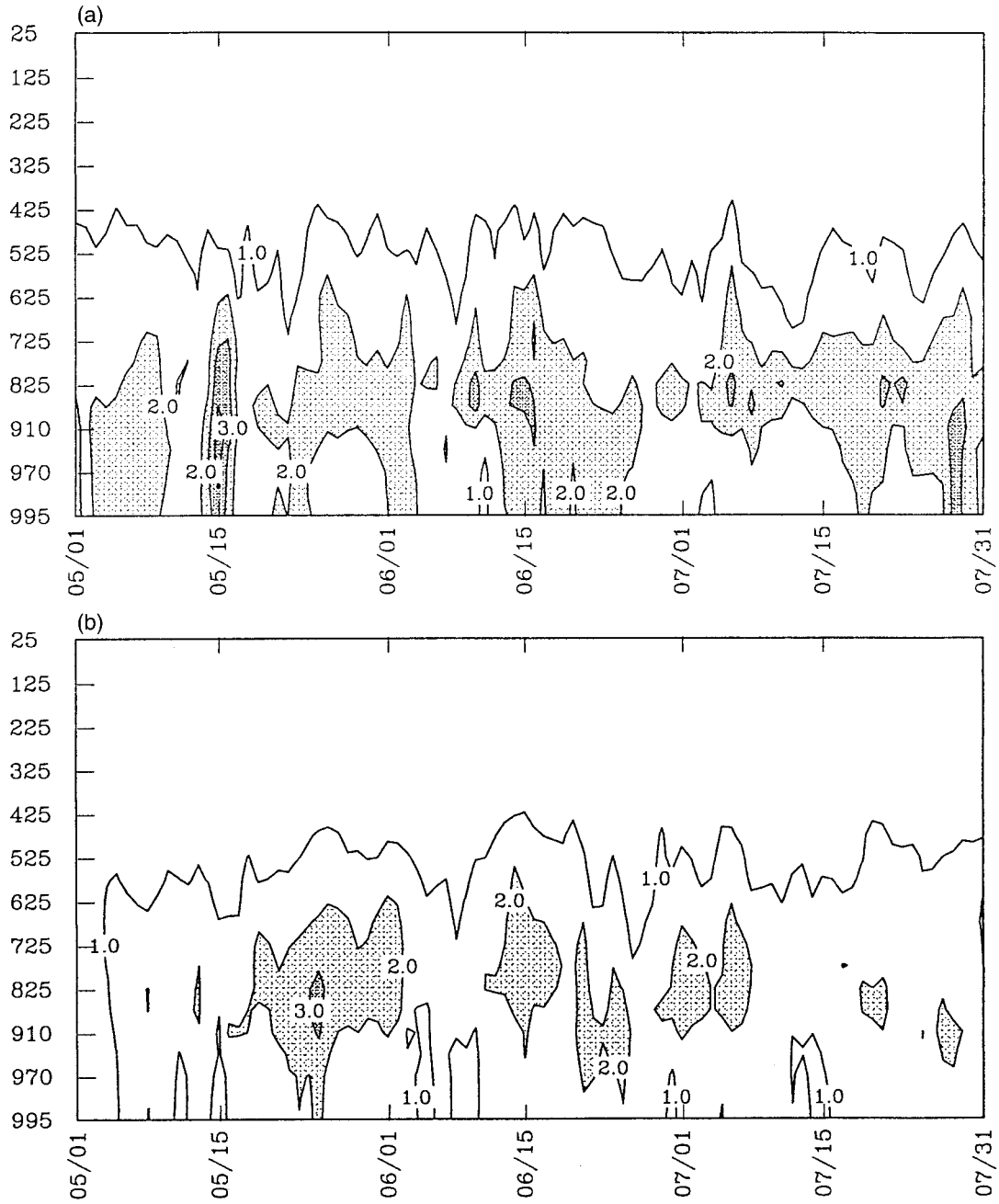

FIG. 8. Rms difference in water vapor mixing ratio (g kg^{-1}) averaged over the inner domain (excluding the 18-gridpoint buffer zone; see Fig. 4 of Wang et al. 2000) for (a) between the model and the corresponding objective analysis for case A, and (b) between the model simulations of cases A and C. Contours greater than 2.0 (3.0) are lightly (densely) shaded.

ferent underlying surface types, that is, ocean versus land, in the above two regions. During the simulation, observed sea surface temperature is used, and therefore the air above the ocean is mainly influenced by changes of radiative heating. On the other hand, the atmosphere over the northern part of the domain is affected, through the larger low cloud, by changes in not only the surface temperature but also the radiative heating. In general, the cloud–radiation interaction due to excessive low clouds resulted in the large model errors in the geopotential height and other model variables as discussed below.

For the zonal wind at 850 hPa, case L5I (Fig. 11a) produces similar model error pattern as in case A (Fig. 3). Note that the model error with maximum of 4–6 m s^{-1} still exists in the northern part of the domain, which is similar to the pattern of difference in 500-hPa geopotential height discussed above. For the cases when

TABLE 2. Designation of sensitivity experiments for different coupling scheme (beffer zone width and nudging coefficient distribution), and treatment of inversion stratus. the ECMWF–TOGA analysis (for case A in Table 1) is used as the driving field.

Designation	Nudging coefficient distribution	Buffer zone width	Inversion stratus
E18	Exponential	18	No
L5I	Linear	5	Yes
L5	Linear	5	No
L18	Linear	18	No

the inversion stratus is removed (cases E18 and L5 shown in Figs. 11b and 11c, respectively), smaller model error is simulated in the northern part of the domain (especially case E18), although the errors still persist in the central part of the domain. This different pattern of model error between cases E18 and L5 indicates its dependence on the coupling scheme, which will be further addressed below.

Figure 12a shows the model error of 850-hPa water vapor mixing ratio for case L5I. In contrast to the model error over the western Pacific Ocean as found in case A (Fig. 4a), substantial increases of model errors near the southern boundary and the middle of the eastern boundary are identified. These increased errors are caused by the steep change of nudging coefficients in the buffer zone, which amplify the difference between model-simulated water vapor and that of the ECMWF–TOGA analysis. This feature, discussed in Giorgi and Mearns (1991), was further explored here, by conducting a 1-month sensitivity experiment with exponentially distributed nudging coefficients using a 10-gridpoint (instead of 18-gridpoint) buffer zone. The result (not shown) shows that the abrupt change of the coefficients at the innermost gridpoint in the buffer zone introduces similar error in water vapor mixing ratio after 9 days of integration, just as in the case L5I. This shows the importance of smooth nudging coefficient in the treatment of the water vapor field, especially for those regions where model error is sensitive to the difference between the model-predicted variables and the corresponding objective analysis.

When the inversion stratus was removed, both E18 and L5, shown in Figs. 12b and 12c, respectively, indicate significantly smaller model error in water vapor mixing ratio over the northern part of the domain. Over the central part of the domain, case E18 produces less model error than case A, whereas case L5 even amplifies the error found in case L5I over some regions (e.g., south of Japan). The large model errors of water vapor in cases L5I and L5 are mainly caused by the propagation of spurious water vapor generated near the southern and eastern boundaries. Again, similar to the 850-hPa zonal wind, model errors of water vapor exist in cases L5 and E18, in particular over the central part of the domain. Because these errors vary among different cases, they can be attributed to the coupling scheme.

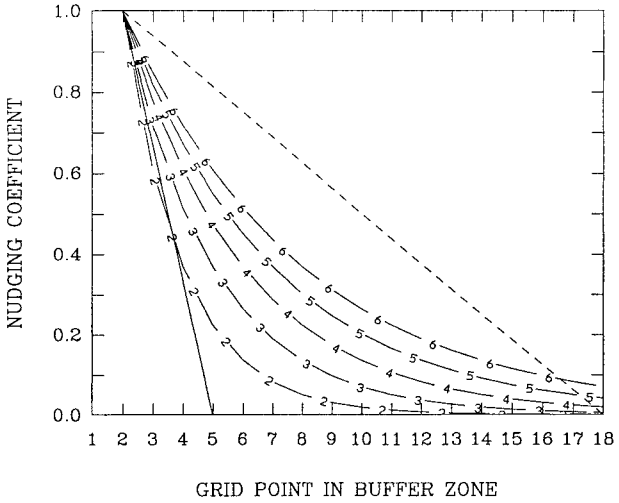

FIG. 9. The distributions of nudging coefficient used in the coupling scheme: (solid line) linear function with 5-gridpoint buffer zone; (short dashed line) linear function with 18-gridpoint buffer zone; and (dashed line with numbers) exponential function with 18-gridpoint buffer zone. The numbers in the lines correspond to ''NI'' used in Eq. (11) of Giorgi et al. (1993b). Here NI is the weight of the nudging coefficient with larger value implying stronger nudging.

To further investigate how the coupling scheme affects the model error, another experiment, designated as L18 (see Table 2), was conducted with the same condition as in case E18 except using larger linearly distributed nudging coefficients (see short dashed line in Fig. 9). Note that the artificial nudging effect in case L18 is applied only to the lateral buffer zone. Therefore, the difference between the two cases is that L18 forces more information of the driving field to reach the boundaries of the inner domain than the case of E18. The motivation here is to examine whether the model-simulated variables inside the inner domain are closely related to the information of the driving field that reaches the boundaries of the inner domain. It is found that the model error of 850-hPa zonal wind over the central part of the domain identified in case E18 (Fig. 11d) is substantially reduced in case L18. In addition, the model error of 850-hPa water vapor mixing ratio is also reduced over this region (see comparison between Figs. 12d and Fig. 12b).

These results indicate that the RCM needs adequate large-scale information near the boundaries of the inner domain, thus highlighting the importance of the nudging coefficients within the buffer zone. These certainly raise the issues of model dynamics and physical parameterization. Of course, as indicated by Errico and Baumhefner (1987), the regional model itself has an inherent weakness constrained by the limited domain in describing the large-scale information, that is, the amplitude and phase as well as its time evolution. In addition to the influence of individual scales beyond this limitation on regional model simulation, there still exist interactions among different scales (Errico 1985), which may

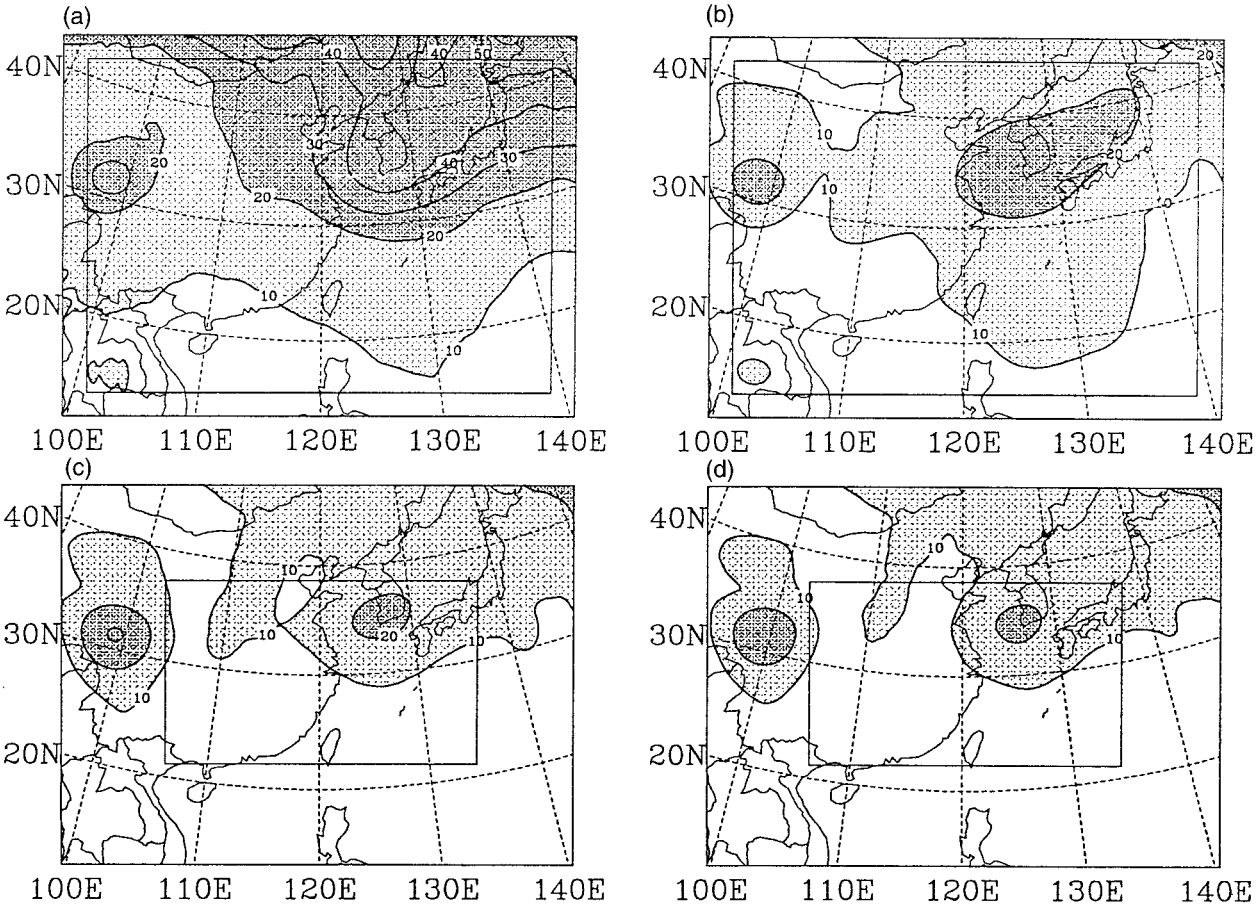

FIG. 10. The May monthly mean absolute value of daily differences in large-scale component of 500-hPa geopotential height (gpm) between the model simulations and ECMWF–TOGA analysis. The four cases, (a) case L5I, (b) case L5, (c) case E18, and (d) case L18 are listed in listed in Table 2. Contours greater than 10 (20) gpm are lightly. (densely) shaded. Rectangular frames in (a) and (c) denote the 5-gridpoint buffer zone.

also play an important role in influencing the domain simulation. Nevertheless, for the few cases studied here, it is clear that the larger the buffer zone (E18 vs L5) and the stronger the nudging (L18 vs E18) the more large-scale information can be mapped onto the domain with subsequent better simulations.

It is therefore reasonable to conclude that, for the LBC method, a larger buffer zone and larger and smoothly varying nudging coefficients should be applied outside the focused area. In so doing, more large-scale information, including the information beyond the scale of the upper limit that can be resolved by the simulation domain, can be provided to the boundaries surrounding the interested area. This strategy, however, suffers from reducing the effective simulation results in the sense that the outputs within the buffer zone have limited use. Note that providing more large-scale information to the interested area cannot be achieved by simply reducing the domain size because steep variation of nudging coefficients in the buffer zone would also induce large error in water vapor mixing ratio, as shown in cases L5I and L5. This is also true for 200-hPa winds. These results were consistent with previous studies of Dickinson et al. (1988) and Trendon and Peterson (1993), who showed simulation error increases with decrease of the domain size.

To further study the influences of different coupling schemes and stratus clouds on large-scale circulation, we analyze the spectra of some variables using the approach developed by Errico (1985). Similar procedure was also used by Waldron et al. (1996) to evaluate model sensitivity to both the LBC and SBC schemes. Figure 13 shows the spectra of May monthly mean 850-hPa zonal wind of the different cases using different coupling schemes, with and without inversion stratus. Note that the differences in variance at different wavenumbers cannot be directly compared with each other because of their different scales. There are several points worth comment. Using the objective analysis as references, the model errors associated with large-scale circulation for each case can be clearly seen in this plot; cases L5I and L5, with smaller buffer zone and weaker nudging, produce larger error than those in cases A and E18. Case L5, with smaller buffer zone width and weak-

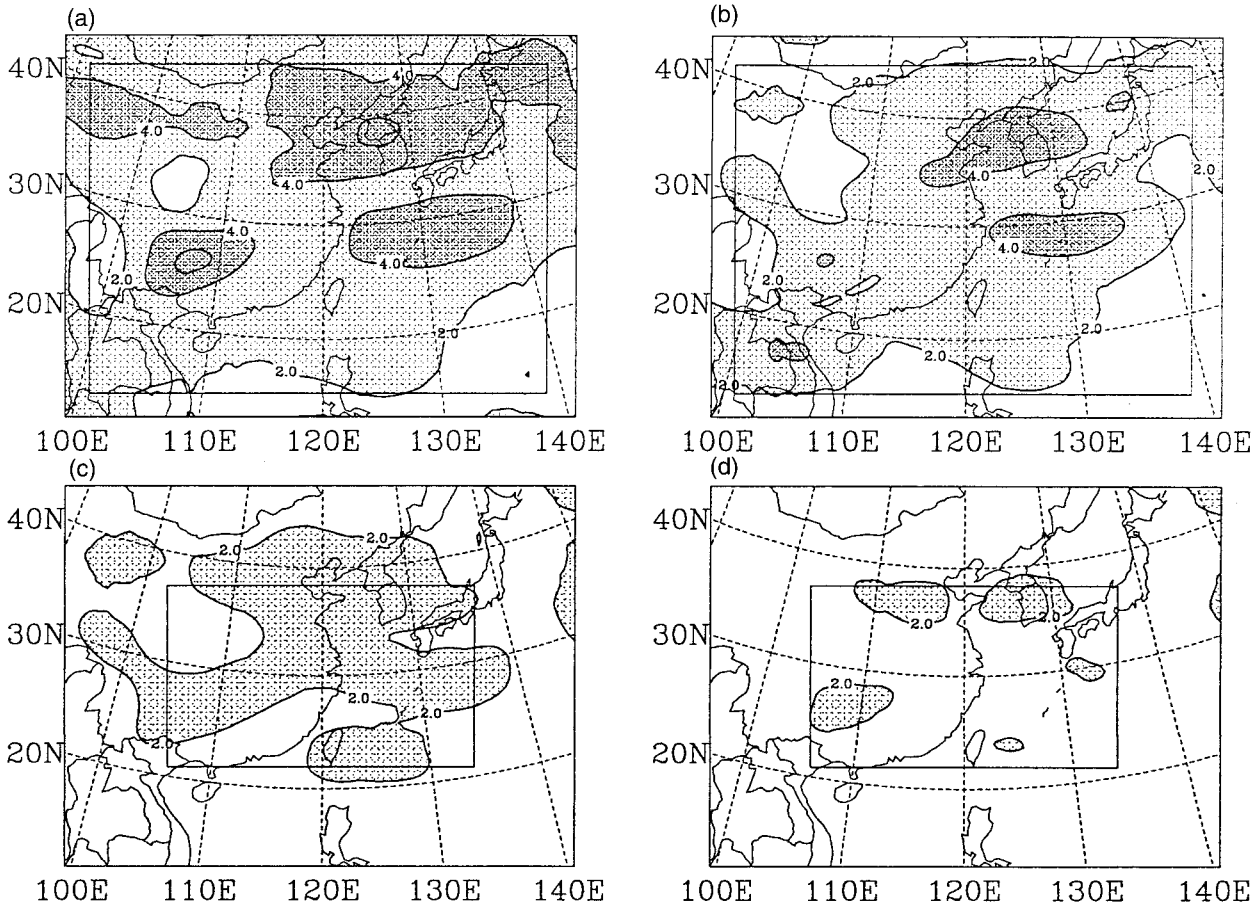

FIG. 11. Same as in Fig. 10 except for 850-hPa zonal wind (m s^{-1}). Contours greater than 1.0 (2.0) m s^{-1} are lightly (densely) shaded.

er nudging, can produce even better results than case A at lower wavenumbers (i.e., on the large scale). This indicates the importance of model physics in improving the simulation. Similar results are found in the spectra of 850-hPa meridional wind and 500-hPa geopotential height (not shown). The small-scale variance at higher wavenumbers (greater than 18 or wavelength less than 280 km for the simulation domain) is larger for all cases than that of objective analysis, indicating that the stronger small-scale information is indeed generated using the regional model. The feature was also demonstrated in Pan et al. (1998). Of course, some small-scale information is suppressed in case L18 in the buffer zone because of the strong nudging. It is interesting to note that removing the inversion stratus also leads to a decrease in small-scale information. However, we cannot judge whether some of the small-scale information is wrongly generated by the parameterization of inversion stratus because the information is lacking from observation. Finally, case L18 produces the closest spectra among these runs to that of ECMWF–TOGA analysis, especially below wavenumber 6. This further illustrates that the larger buffer zone and stronger nudging can be used to obtain similar results as that using the SBC method, but without encountering the problem of discontinuity mentioned earlier.

Clearly, given the stated strategy for LBC method, it needs to address the issue of whether the small-scale information over the inner domain is affected by the artificial nudging in the buffer zone. Here, we analyze its influence on the spectra while more analysis and statistics will be given in section 4b. Figure 14 shows the spectra of the 850-hPa zonal wind within the inner domain for the considered cases. It is found that there is very little difference in the variance among the cases with the same diagnostic cloud–radiation parameterization. Note that the wavelengths are reduced because the spectral analysis is performed for the inner domain. The differences among these cases over the inner domain are mainly stored in the linear trend field, which has been removed before Fourier transform is performed. This indicates the spectra for the inner domain depend only on the model physics, but not on the treatment of coupling schemes in the buffer zone. The same conclusion can be drawn for the corresponding spectra of 850-hPa water vapor mixing ratio (not shown). However, unlike zonal wind, the plotted variance at each wavenumber for water vapor mixing ratio is not sig-

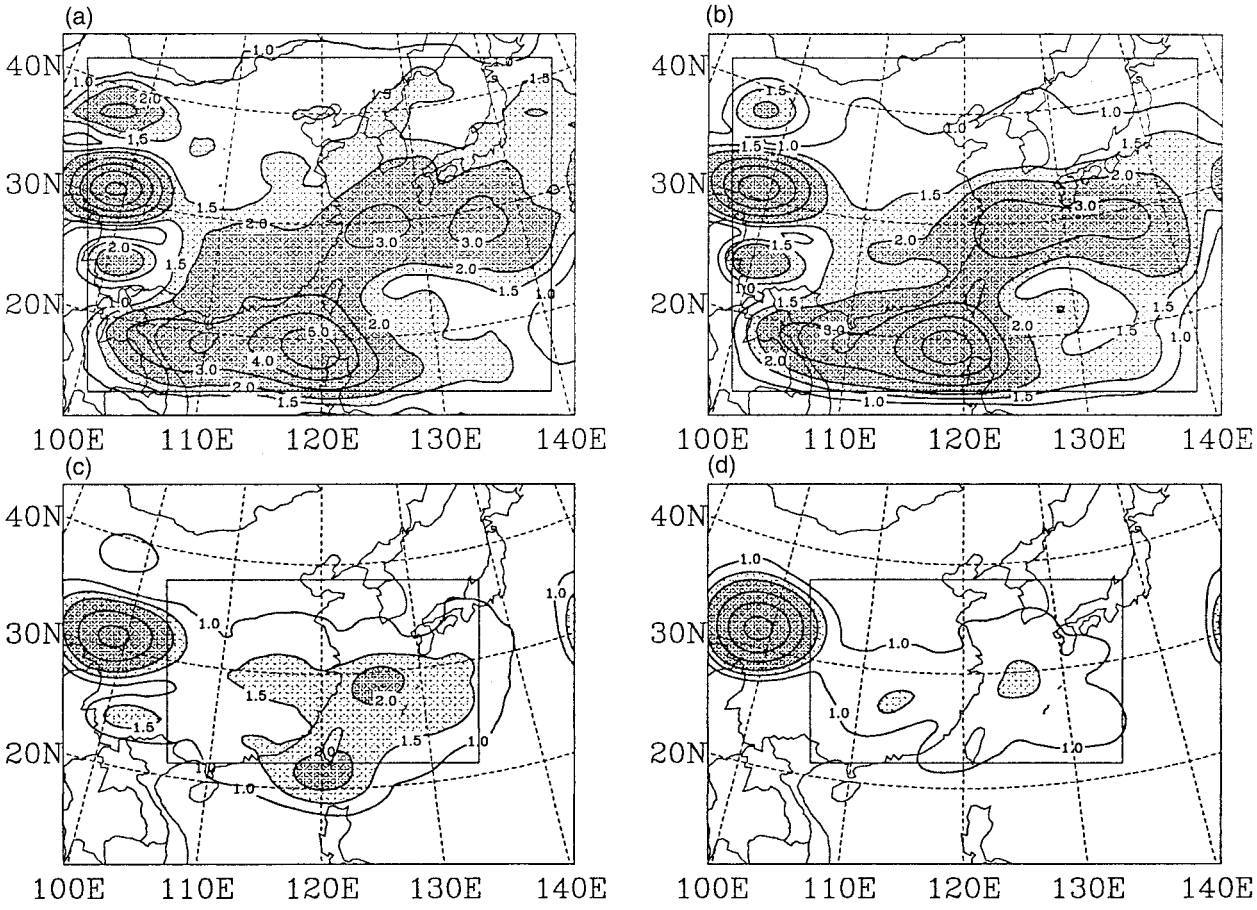

FIG. 12. Same as in Fig. 10 except for 850-hPa water vapor mixing ratio (g kg^{-1}). Contours greater than 1.5 (2.0) g kg^{-1} are lightly (densely) shaded.

nificantly affected by the diagnostic cloud–radiation parameterization. The result is consistent with previous comparison of Fig. 12a with Fig. 12c.

b. Mesoscale signals

It is also important to examine the influence of nudging on the mesoscale signals. As indicated by Giorgi et al. (1993), the topographic signal, which is one of the key mesoscale signals that can be found in the high-resolution model, can be characterized by the spatial standard deviation. Figure 15 depicts the variation of spatial standard deviation of precipitation (see Wang et al. 2000) using all available surface stations within the region (23°–43°N; 105°–122°E) for cases L5, E18, and L18 and observation. The observed trend has two peaks and one minimum in the month of May. In general, all three experiments catch the observed characteristics except for the 24 May maximum. In the first 8 days of integration, L5 produces better simulation than the other two experiments, but it is the worst for the rest of the month, especially during the period of 15–23 May. The spatial standard deviations of surface air temperature (not shown) are not significantly different among these three cases, which all capture reasonably well the trend of observation for the month. The comparisons further demonstrate that the mesoscale signals over the inner domain are not significantly affected by the nudging procedure.

In addition, we calculated the rms error of precipitation and surface air temperature for all stations over three latitudinal zones, using Eq. (6). [Note that Wang et al. (2000) show the errors in three latitudinal zones, Northern China, YHRV, and Southern China.] The precipitation rms errors for L18 (see Fig. 16) are smaller than the other two experiments during 4–10 May over the South China region, thus explaining the differences of total precipitation among these sensitivity experiments. On the other hand, over YHRV, the differences of the rms errors are small (see Fig. 17). In addition, the rms error of temperature calculated for all stations in L5 are greater than in the other two cases.

The geographical distribution of observed May monthly mean precipitation along with the simulations for cases L5, E18, and L18 are shown in Fig. 18. The observation shows two regions with precipitation values

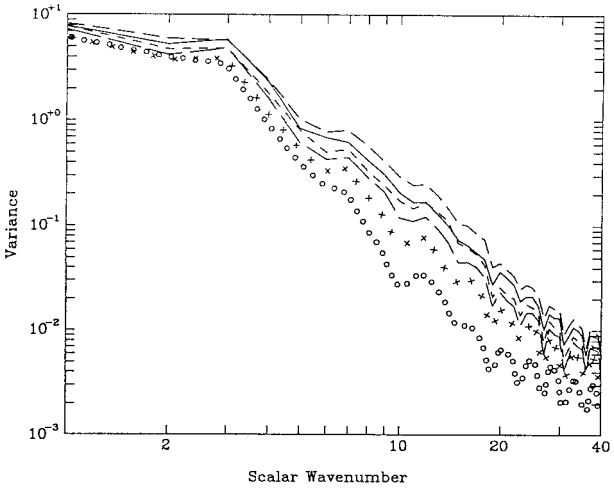

FIG. 13. Spectra of variance (logarithm) of 850-hPa zonal wind as a function of scalar wavenumber (see Errico 1985) for ECMWF–TOGA analysis and sensitivity experiments on the treatment of coupling scheme and of inversion stratus. Fourier expansion are performed over the entire integration domain. Here "○" is for ECMWF–TOGA analysis, "×" for case L18, solid line for case A, long dashed line for case E18, middle dashed line for case L5I, and short dashed for case L5.

exceeding 6 mm day^{-1}, one along YHRV and the other over southeast China. The largest precipitation center is located over the Yangtze River valley with 9 mm day^{-1}, which occurred during the pre-Mei-yu season 18–27 May (Ding 1993). It is quite clear that case L5, because of the largest model error in both lower-tropospheric wind and water vapor, simulates the worst pattern. For case E18, improvement is found over southeast China, and the middle reach of the Yangtze River, although their intensities are still not well simulated. With stronger nudging in the buffer zone, L18 catches reasonably well the observed precipitation pattern, especially the

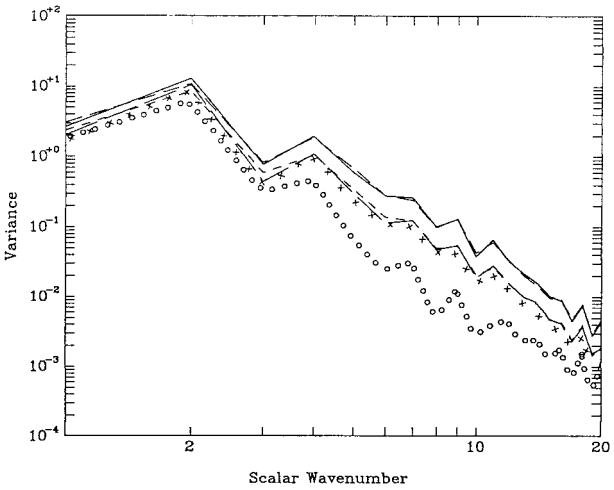

FIG. 14. Same as in Fig. 13 except for the inner domain (i.e., excluding 18-grid point near the lateral boundaries).

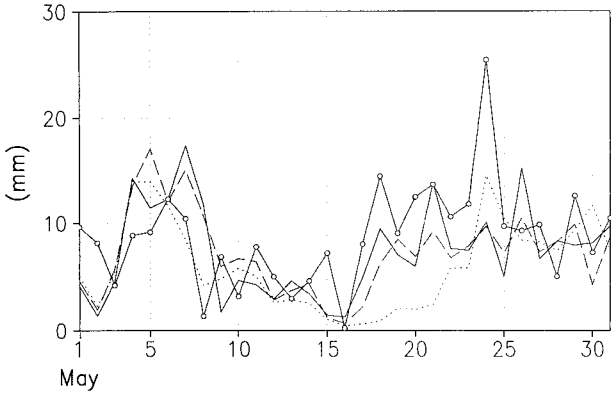

FIG. 15. Time variation of spatial standard deviation of precipitation calculated for stations between 105°–122°E and 23°–43°N. Solid line with open circle is for observation, dot for L5, dashed line for E18, solid line for L18.

structure over YHRV, for example, the L-shaped rainfall pattern. Further evidence of the improvement is found in the monthly and regional mean statistics, as shown, respectively, in Tables 3 and 4. Of these three experiments, the statistics of precipitation are improved with the increase of buffer zone width and nudging coefficients. The error of monthly mean precipitation is reduced by 0.59 mm day^{-1} (16% of the observed 3.76 mm day^{-1}) in L18 when compared with L5. In addition, the spatial correlation is substantially improved in L18, which is consistent with those shown in Fig. 18. However, the simulation of monthly mean surface air temperature becomes slightly worse with the increase of buffer zone width and nudging coefficient. Note that when compared with L5, both the spatial and temporal correlation are slightly improved in L18 and E18.

The effect on precipitation due to removing the inversion stratus was also examined. However, for at least two reasons, no significant improvement is observed. First, the inversion stratus did not form frequently over YHRV, where extremely unstable air persists during the

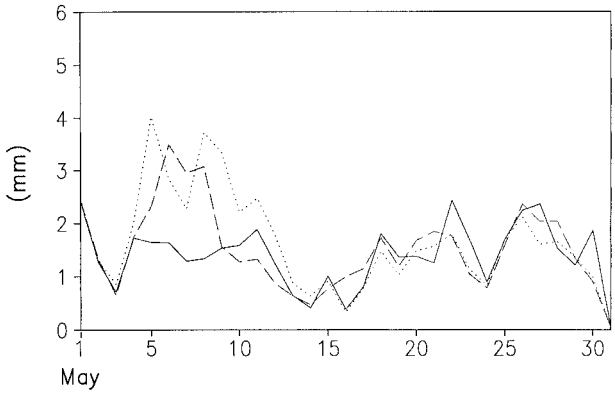

FIG. 16. The rms error between simulated and observed precipitation calculated for stations between 23°–43°N and 105°–122°E. Dot is for L5, dashed line for E18, solid line for L18.

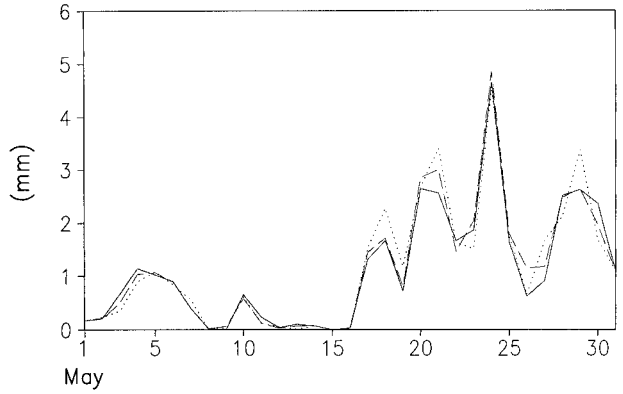

FIG. 17. Same as in Fig. 16 but for stations between 30°–34°N and 105°–122°E.

period of integration. Second, lower-level wind error, partly due to the use of coupling scheme, is still large in the inner domain, thus resulting in no change in the convergence region. These outcomes are in sharp contrast with the effect of the coupling scheme. When more large-scale information of the driving field is imposed outside the inner domain by stronger nudging, as in case L18, model errors of both wind and water vapor mixing ratio are reduced, so that the drift problem is prevented and realistic precipitation pattern is simulated.

TABLE 3. Statistics of simulated 1991 May precipitation within the region 23°–43°N; 105°–122°E). Here Er denotes monthly mean error; Cs and Ct are spatial and temporal correlations, respectively (see Wang et al. 2000).

Experiment	Er (mm day^{-1})	Cs (%)	Ct (%)
L5	−0.76	27.69	73.67
E18	−0.19	37.45	74.40
L18	−0.17	42.22	75.07

5. Conclusions and discussion

In this study, we used the SUNYA–RCM to examine the model bias associated with the treatment of lateral boundary conditions (driving fields and coupling scheme). In addition, the effect of inversion stratiform clouds is also investigated. Analyses of the bias were based on sensitivity experiments of the 1991 severe summer precipitation event over East Asia. Note that we define here the model bias associated with the lateral

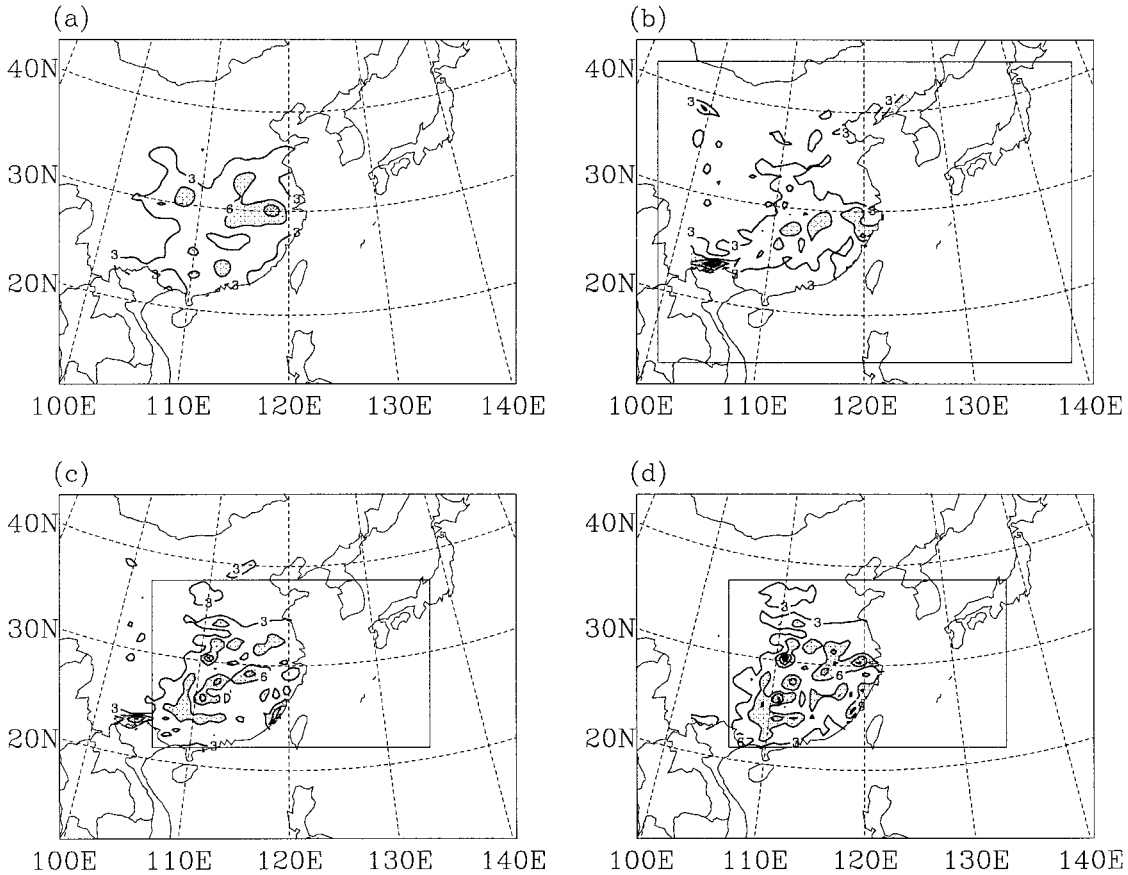

FIG. 18. The 1991 May monthly mean precipitation (mm day^{-1}) over continental China. (a) Observation from WMO surface station network (383 stations), (b) case L5; (c) case E18, and (d) case L18. Contours greater than 6.0 (9.0) mm day^{-1} are lightly (densely) shaded.

TABLE 4. Same as in Table 3 but for surface air temperature.

Experiment	Er (°C)	Cs (%)	Ct (%)
L5	−0.02	94.35	92.96
E18	0.13	96.80	93.71
L18	0.31	96.32	94.26

boundary as the model uncertainties that are different from the model errors associated with the model itself (e.g., the coupling scheme and model physical parameterization). The results indicate that uncertainties associated with the driving fields can significantly affect the 850-hPa zonal and meridional winds, 500-hPa geopotential height, and 850-hPa water vapor mixing ratio; all are important in simulating the monsoon evolution over East Asia. However, the precipitation variability and pattern using different driving fields show only minor differences.

The coupling scheme has considerable influence on circulation, especially the 850-hPa water vapor mixing ratio, and 200-hPa zonal and meridional winds. In contrast to the driving fields, the simulated monthly mean precipitation and its spatial pattern are sensitive to the coupling scheme. This suggests the need to use a larger buffer zone with stronger and smoother nudging coefficients in order to provide sufficient large-scale information to the interested area. This treatment avoids the problem of discontinuity of prognostic variables associated with the spectral boundary coupling scheme and yields similar coupling effects as the spectral coupling scheme. However, other problems exist. For example, stronger nudging brings into the simulation domain uncertainties inherent in the driving fields and also, to some extent, reduces the spatial domain where simulation results are useful. In addition, problems in the model numerics and physics within the buffer zone may also be concealed.

Excessive low-level clouds, which is related to the inversion stratus in the diagnostic cloud–radiation parameterization adopted in the model, has been identified to introduce large model error. Simple sensitivity experiment of eliminating the inversion stratus reduces to some extent the colder and drier bias of the model atmosphere occurring over the northern part of the simulation domain. Since the SUNYA-RCM was originally applied to the Southern Great Plains of the United States (Dudek et al. 1996), inherently the model includes some of the characteristics pertinent to that particular region. Consequently, physical parameterization needs to be carefully evaluated when the model is used for other regions with distinctively different climate characteristics. In any case, parameterization for cloud–radiation interaction perhaps is the most important aspect that needs improvement in modeling regional climate. This was also clearly illustrated in an intercomparison study (Leung et al. 1999) of three different regional climate models, including the SUNYA-RCM.

Finally, an analysis of spectra of several simulated variables indicates that the model is capable of producing small-scale features with specified large-scale driving fields and use of nudging coefficients, thus suggesting the potential of using the model to study regional climate with inherent regional characteristics. Moreover, the small-scale components over the inner domain are not strongly influenced by the coupling schemes, further indicating the appropriateness of using a wider buffer zone.

Acknowledgments. The research was supported by Biological and Environmental Research, Office of Science, U.S. Department of Energy.

REFERENCES

Anthes, R. A., E. Y. Hsie, and Y. H. Kuo, 1987: Description of the Penn State/NCAR Mesoscale Model version 4 (MM4). NCAR Tech. Note NCAR/TN-282+STR, National Center for Atmospheric Research, Boulder, CO, 66 pp. [Available from NCAR, P.O. Box 3000, Boulder, CO 80307.]

——, Y. H. Kuo, E. Y. Hsie, S. Low-Nam, and T. W. Bettge, 1989: Estimation of episodic and climatological skill and uncertainty in regional numerical models. *Quart. J. Roy. Meteor. Soc.*, **115,** 763–806.

Bony, S., Y. Sud, K.-M. Lau, J. Susskind, and S. Saha, 1997: Comparison and satellite assessment of NASA/DAO and NCEP–NCAR reanalyses over tropical ocean: Atmospheric hydrology and radiation. *J. Climate,* **10,** 1441–1462.

Davies, H. C., 1976: A lateral boundary formulation for multilevel prediction models. *Quart. J. Roy. Meteor. Soc.*, **102,** 405–418.

Dickinson, R. E., R. M. Errico, F. Giorgi, and G. T. Bates, 1988: Modeling of historic, prehistoric and future climates of the Great Basin. NCAR Final Rep. to USGS/NNWSI, 46 pp. [Available from NCAR, P.O. Box 3000, Boulder, CO 80307.]

Ding, Y.-H., 1993: *Research on the 1991 Persistent, Severe Precipitation over Yangtze–Huai River Valley* (in Chinese). Chinese Meteorological Press, 255 pp.

Dudek, M. P., X.-Z. Liang, and W.-C. Wang, 1996: A regional climate model study of the scale dependence of cloud–radiation interactions. *J. Climate,* **9,** 1221–1234.

Errico, R. M., 1985: Spectra computed from a limited area grid. *Mon. Wea. Rev.,* **113,** 1554–1562.

——, and D. Baumhefner, 1987: Predictability experiments using a high-resolution limited-area model. *Mon. Wea. Rev.*, **115,** 488–504.

Giorgi, F., 1990: On the simulation of regional climate using a limited area model nested in a general circulation model. *J. Climate,* **3,** 941–963.

——, and L. O. Mearns, 1991: Approaches to the simulation of regional climate change: A review. *Rev. Geophys.,* **29,** 191–216.

——, G. T. Bates, and S. Nieman, 1993a: The multiyear surface climatology of a regional atmospheric model over the western United States. *J. Climate,* **6,** 75–95.

——, M. R. Marinucci, and G. T. Bates, 1993b: Development of a second-generation regional climate model (RegCM2). Part II: Convective processes and assimilation of lateral boundary conditions. *Mon. Wea. Rev.,* **121,** 2814–2832.

Kida, H., T. Koide, H. Sasaki, and M. Chiba, 1991: A new approach for coupling a limited area model to a GCM for regional climate simulations. *J. Meteor. Soc. Japan,* **69,** 723–728.

Kiehl, J. T., 1994: Sensitivity of a GCM climate simulation to differences in continental versus maritime cloud drop size. *J. Geophys. Res.,* **99,** 23 107–23 115.

Liang, X.-Z., and W.-C. Wang, 1995: A GCM study of the climatic effect of 1979–1992 ozone trend. *Atmospheric Ozone as a Cli-*

mate Gas, NATO ASI Series, W.-C. Wang and I. S. A. Isaksen, Eds., Springer-Verlag, 259–288.

Leung, L. R., S. J. Ghan, Z.-C. Zhao, Y. Luo, W.-C. Wang, and H.-L. Wei, 1999: Intercomparison of regional climate simulations of the 1991 summer monsoon in East Asia: Special issue on ''New Development and Applications in Regional Climate Models.'' *J. Geophys. Res.*, **104,** 6425–6454.

Min, W., and S. Schubert, 1997: The climate signal in regional moisture fluxes: A comparison of three global data assimilation products. *J. Climate,* **10,** 2623–2642.

Mo, K. C., J. N. Paegle, and J. Paegle, 1995: Physical mechanisms of the 1993 summer floods. *J. Atmos. Sci.,* **52,** 879–895.

Pan, Z.-T., E. Takle, W. Gutowski, and R. Turner, 1999: Long simulation of regional climate as a sequence of short segments. *Mon. Wea. Rev.,* **127,** 308–321.

Sasaki, H., H. Kida, T. Koide, and M. Chiba, 1995: The performance of long-term integrations of a limited area model with the spectral boundary coupling method. *J. Meteor. Soc. Japan,* **73,** 165–181.

Slingo, A., and J. M. Slingo, 1991: Response of the National Center for Atmospheric Research Community Climate Model to improvements in the representation of clouds. *J. Geophys. Res.,* **96,** 15 341–15 347.

Tao, S.-Y., and L.-X. Chen, 1987: A review of recent research on the East Asian summer monsoon in China. *Monsoon Meteorology,* C.-P. Chang and T. N. Krishnamurti, Eds., Oxford University Press, 60–92.

Tatsumi, Y., 1986: A spectral limited-area model with time-dependent lateral boundary conditions and its application to a multi-level primitive equation model. *J. Meteor. Soc. Japan,* **64,** 637–663.

Trenberth, K. E., and C. J. Guillemot, 1995: Evaluation of the global atmospheric moisture budget as seen from analyses. *J. Climate,* **8,** 2255–2272.

Trendon, R. E., and R. A. Petersen, 1993: Domain size sensitivity experiments using the NMC Eta model. Preprints, *13th Conf. on Weather Analysis and Forecasting,* Vienna, VA, Amer. Meteor. Soc., 176–177.

Vukicevic, T., and R. M. Errico, 1990: The influence of artificial and physical factors upon predictability estimates using a complex limited-area model. *Mon. Wea. Rev.,* **118,** 1460–1482.

Waldron, K. M., J. Paegle, and J. D. Horel, 1996: Sensitivity of a spectrally filtered and nudged limited-area model to outer model options. *Mon. Wea. Rev.,* **124,** 529–547.

Walsh, K., and I. G. Watterson, 1997: Tropical cyclone-like vortices in a limited area model: Comparison with observed climatology. *J. Climate,* **10,** 2240–2259.

Wang, W.-C., W. Gong, and H. Wei, 2000: A regional model simulation of 1991 severe precipitation event over the Yangtze–Huai River Valley. Part I: Precipitation and circulation statistics. *J. Climate,* **13,** 74–92.

Warner, T. T., R. A. Peterson, and R. E. Treadon, 1997: A tutorial on lateral boundary conditions as a basic and potentially serious limitation to regional numerical weather prediction. *Bull. Amer. Meteor. Soc.,* **78,** 2599–2617.